Editors' Suggestion

Parity and Singlet-Triplet High-Fidelity Readout in a Silicon Double Quantum Dot at 0.5 K

David J. Niegemann,[1,*] Victor El-Homsy,[1] Baptiste Jadot,[1] Martin Nurizzo,[1]
Bruna Cardoso-Paz,[1] Emmanuel Chanrion,[1] Matthieu Dartiailh,[1] Bernhard Klemt,[1] Vivien Thiney,[1]
Christopher Bäuerle,[1] Pierre-André Mortemousque,[2] Benoit Bertrand,[2] Heimanu Niebojewski,[2]
Maud Vinet,[2] Franck Balestro,[1] Tristan Meunier,[1] and Matias Urdampilleta[1,†]

[1] *Université Grenoble Alpes, CNRS, Grenoble INP, Institut Néel, Grenoble 38402, France*
[2] *CEA, LETI, Minatec Campus, Grenoble F-38054, France*

(Received 8 July 2022; revised 22 September 2022; accepted 8 November 2022; published 26 December 2022)

Pauli-spin-blockade (PSB) measurements have so far achieved the highest fidelity of spin readout in semiconductor quantum dots, overcoming the 99% threshold. Moreover, in contrast to energy-selective readout, PSB is less error prone to thermal energy, an important feature for large-scale architectures that could be operated at temperatures above a few hundreds of millikelvins. In this work, we use rf reflectometry on a single-lead quantum dot to perform charge sensing and to probe the spin state of a double quantum dot at 0.5 K. At this relatively elevated temperature, we characterize both singlet-triplet and parity readout, which are complementary measurements to perform a complete readout of a two-spin system. We demonstrate high-fidelity spin readout with an average fidelity above 99.9 % for a readout time of 20 µs and 99 % for 4 µs. Finally, we succeed in initializing a singlet state in a single dot with a fidelity higher than 99 % and separate the two electrons while retaining the same spin state with a 95.6 % fidelity.

DOI: 10.1103/PRXQuantum.3.040335

I. INTRODUCTION

The system size of today's semiconductor quantum dot qubits remains in the few-qubits regime [1,2] but the community is already working on scalable designs for qubit processors [3]. Scaling up qubit systems goes along with an increased interest in cointegration of control electronics [4,5]. This would result in higher power dissipation at the quantum chip level and the necessity to work at elevated temperatures (beyond the dilution fridge base temperature), where the cooling power is typically in the hundreds of milliwatts range [6]. Important progress in this direction has been made, namely the realization of high-fidelity single-qubit gates and two-qubit gates [7–9] above 1 K. However, the spin-readout infidelity increases with increasing temperature due to thermal broadening of the charge sensor [6,7]. Moreover, above 0.5 K, the spin dynamics are degraded: the relaxation rates increase due to an increase in the phonon population and in two-phonon processes [10] and decoherence rates increase due to coupling to stronger charge noise [7].

For temperatures higher than the Zeeman energy, the method of choice to perform spin readout relies on Pauli spin blockade (PSB). PSB-based readout has so far shown the highest readout fidelity, achieving fidelities >99 % [11,12] and the highest operating temperatures, as high as 4.5 K [8]. This allows us to probe a two-spin system and to distinguish between the singlet state S_0 and the triplet states T_-, T_0, and T_+. As PSB just provides one bit of information, another readout mechanism or a single-qubit manipulation is required to determine the system state completely [13]. In this context, PSB-based parity measurements yield another bit of information by discriminating the unpolarized spin states (S_0 and T_0) from the polarized ones (T_+ and T_-) [1,14]. Using a combination of standard PSB [also called singlet-triplet (S-T) readout in the following] and parity readout allows us to distinguish each of the T_0, S_0, and T_- (T_+) states, a requirement for the full tomography of a two-spin-1/2 system [13,15]. Achieving high-fidelity spin readout requires a charge detector with a strong capacitive coupling. The standard charge sensor in many devices is a single-electron transistor or quantum point contact, with at least three leads [1,7,9,16]. This large contact overhead poses scalability challenges, especially if one wants to have local charge sensors in

---

[*] david.niegemann@neel.cnrs.fr

[†] matias.urdampilleta@neel.cnrs.fr

two-dimensional (2D) arrays [17]. A solution is rf reflectometry, which does not rely on a resistive measurement but on a capacitive measurement [18]. This allows us to reduce the sensor device to a single-lead quantum dot [11,19–21].

In this work we combine, at relatively elevated temperature, scalable fabrication technology, PSB, and rf-reflectometry on a single-lead quantum dot to demonstrate rapid and high-fidelity single-shot readout of spins in a double quantum dot. We choose to operate the device at a temperature of 0.5 K, where the spin dynamics are still unaltered by phonon or charge noise [1,10]. This is also motivated by the recent development of cryogenic apparatuses, such as wafer-scale cryoprobers, using Joule-Thomson ^{3}He cryocoolers, which provide much higher cooling power than dilution refrigerators. Despite the relatively high temperature, we obtain average fidelity and visibility exceeding 99 % at a 4-μs integration time for parity and singlet-triplet readout.

II. DEVICE FABRICATION AND EXPERIMENTAL SETUP

The device used in this work, which is similar to the one depicted in Fig. 1(a), is fabricated on a 300-mm silicon-on-insulator substrate. A 80-nm-wide silicon channel is defined by mesa patterning and is separated from the substrate by a buried oxide of thickness 145 nm. 6-nm thermally grown SiO_2 is used to separate the gates from the nanowire. The gates are made by atomic layer deposition of 5 nm of TiN and 50 nm of poly-Si. A bilayer hard mask of 30-nm SiN and 25-nm SiO_2 is placed on top of the metallic gates. The use of a hybrid deep-UV–electron-beam gate-patterning scheme allows us to transfer the gate structure into the hard mask by an alternation of lithography and etch steps. A final etch step separates the gates, resulting in a total of six gates (2 × 3) of 40 nm in gate width, longitudinal and transverse spacing. Before doping of the reservoirs, Si_3N_4 spacers of thickness 35 nm are deposited to cover the space between the gates. Then, the source and drain reservoirs, labeled S and D respectively, are n-type doped using ion implantation, followed by an activation step using a N_2-spike anneal. Finally, the device is encapsulated and the gates are connected to Al bond pads.

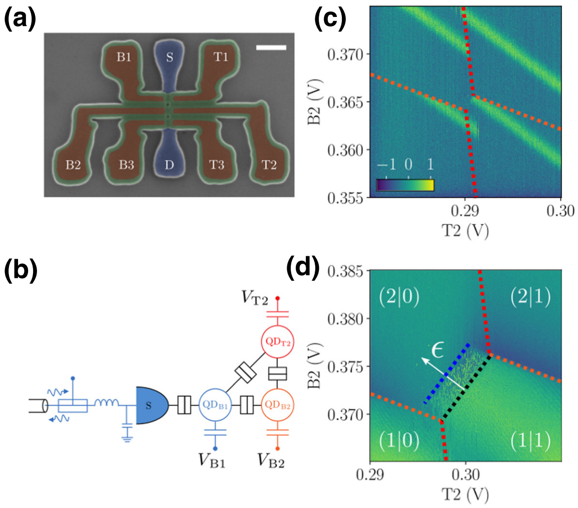

FIG. 1. (a) A false-color SEM micrograph of a device similar to the one used in this work. The quantum dot defining gates (red) are on top of the nanowire (blue) and are separated by spacers (green). The white bar has a length of 200 nm. (b) The equivalent electrical circuit of the device in the measurement configuration used in this work. The reflectometry circuit is connected to the source. Together with quantum dot QD_{B1}, they form an electrometer. Sensor QD_{B1} is tunnel and capacitively coupled to QD_{B2} and QD_{T2}, allowing their charge state to be sensed. (c) The stability diagram of the two quantum dots, QD_{B2} and QD_{T2}. A charge transition of QD_{B1} is split horizontally (vertically) by a charge transition of QD_{B2} (QD_{T2}). The orange (red) dotted lines indicate the transition of QD_{B2} (QD_{T2}). (d) The interdot transition of the (2|0)-(1|1) regime at 300 mT. The space between the blue and black dotted lines indicates the PSB region, limited by the energy spacing to the next valley or orbital state.

The device chip is glued to a printed circuit board and all gates except gate B2 are connected to dc wires. Gate B2 is connected to a dc wire and a coaxial cable through a bias tee with a 20-kHz dc cutoff. Connecting the source reservoir to a Nb spiral inductor with L=69 nH forms, together with the parasitic capacitance C_p of the circuit, an LC resonance at $f_{\mathrm{res}} = 1.2$ GHz. We extract from the resonance frequency a parasitic capacitance of $C_p \approx 0.25$ pF. The amplitude and phase of the reflection of a rf tone close to the resonance of the LC circuit changes if the resonance frequency of the circuit is changed. A shift of the resonance frequency occurs when the electrochemical potential μ of the reservoir is aligned with an energy level of a nearby quantum dot and electron tunneling can occur [18,22]. We use quadrature (IQ) demodulation to sense the signal change. Thus, source reflectometry allows sensing of the nearby quantum dots (QDs) defined by gates T1 and B1 (see Appendix A 1).

The device is cooled down in a dilution fridge with a variable temperature control. The present experiment is achieved at a base temperature of 500 mK. At this temperature, applying a positive voltage on the gates results in the accumulation of quantum dots at the Si-SiO_2 interface. We can hence form an array of up to 2 × 3 quantum dots. In this work, we only present data using the leftmost 2 × 2 array.

III. CHARGE SENSING USING rf REFLECTOMETRY

We start tuning the sensor, which is controlled by gate B1. To minimize the tunnel coupling between the sensor and the further probed dot, we try to work with the smallest amount of electrons possible in the dot. However, if the number of electrons is too small, the tunnel coupling between the dot and the lead is weak and the resulting reflectometry signal is not sufficiently strong for fast readout [16,22]. We find that the optimal operation point is the degeneracy between four and five electrons in $\mathrm{QD}_{\mathrm{B1}}$ (for more detail on the tuning of the sensor dot, see Appendix A 1). Operating the sensor at this degeneracy point gives a strong capacitive coupling to nearby quantum dots, which allows the detection of the first electron in the double quantum dot formed by B2 and T2 [19,20]. We observe no broadening of this transition for measurements at 100 mK and 500 mK and assume, therefore, that for temperatures below 500 mK the signal is tunnel broadened.

We now move to the tuning of the double quantum dot formed by B2 and T2. Gates B3 and T3 are set to 0 to isolate the double quantum dot from the drain reservoir. To determine the charge-configuration space of the double quantum dot system, we measure the B2-T2 stability diagram and scan the voltage of sensor B1 in a third dimension. The charge degeneracies of the sensor become visible in the B2-T2 stability diagram as broadened Coulomb peaks (see Appendix A 1). Loading a single electron in $\mathrm{QD}_{\mathrm{B2}}$ leads to a splitting of the sensor signal along the B2 voltage [see the orange lines in Fig. 1(c)]. The transitions of the QD defined by T2 are detected as almost vertical cuts of the sensor signal [see the red line in Fig. 1(c)]. Thus, we can probe the charge occupation of $\mathrm{QD}_{\mathrm{B2}}$ and $\mathrm{QD}_{\mathrm{T2}}$ using $\mathrm{QD}_{\mathrm{B1}}$ and the source-reflectometry signal.

IV. PAULI SPIN BLOCKADE FOR SINGLET-TRIPLET AND PARITY READOUT

We start by identifying the region where Pauli spin blockade can occur. For this, we tune the sensor to probe both dots simultaneously and their interdot transition corresponding to the (2|0)-(1|1) charge states, depicted in Fig. 1(d). Under a magnetic field $B_z = 300$ mT, the T_- state is the ground spin state in the (1|1) regime, whereas S_0 remains the ground state in the (2|0) regime, as sketched in Fig. 2(a). Therefore, by scanning over the interdot transition starting from (1|1), we can identify the PSB region as the dashed extension of the (1|1) charge state beyond the interdot transition on the (2|0) side [see Fig. 1(d)]. This PSB area has a finite width as the blockade is lifted when the detuning energy surpasses the valley or orbital energy separating the T_- (2,0) and T_- (1,1) states. After evaluation of the lever arm as approximately 0.05 eV/V (see Appendix A 6), we can estimate the valley splitting to be around 130 μeV, in agreement with measurements performed in similar devices [23].

By performing pulsed measurement in the PSB area, we can resolve the spin-blockade lifting in real time, as presented in Fig. 2(b) . To investigate further the single-shot spin readout, we perform two different measurements. We refer to these as S-T readout and parity readout. The S-T readout is used to distinguish the singlet state from all triplet states. The parity readout is used to distinguish polarized spin states (or even states T_- and T_+) from unpolarized spin states (or odd states T_0 and S_0) [7].

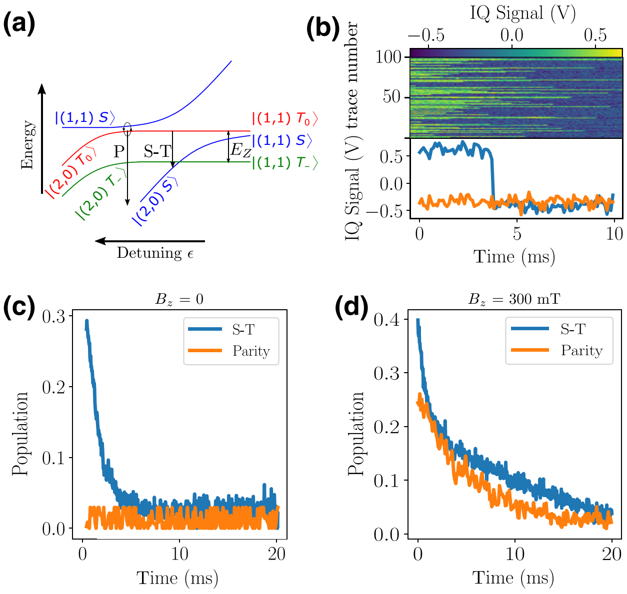

FIG. 2. (a) The energy diagram for the lowest states of the double electron system close to the (2|0)-(1|1) transition at $B_z \neq 0$. The arrow labeled P indicates the position where the T_0 state relaxes rapidly and allows parity readout, whereas the arrow labeled arrow S-T shows the position of the S-T readout. (b) Single-shot measurements of two traces at the parity-readout position: a blocked state relaxing to the nonblocked state in blue and a nonblocked state in orange. (c) The comparison at zero field of the relaxation curves from the mixed triplet states to the nonblocked singlet state measured at the S-T readout (blue curve) and at the parity-readout (orange curve) positions. (d) The comparison at $B_z = 300$ mT of the relaxation curves from the mixed T_- and T_0 states to the singlet state measured at the S-T readout (blue curve) and at the parity-readout (orange curve) positions. The first curve shows a double exponential decay with one fast decay and one slow decay, whereas the second curve just shows a single fast exponential decay.

To characterize the two readout positions separately, we first initialize the spin state in a mixed state of singlet and triplets at zero field. For this, we initialize in the singlet state in (2|0). Subsequently, pulsing to (1|1) results in singlet- and triplet-state mixing (see Appendix A 9). We then pulse the gates to one of the two measurement points. The result of the readout for both the S-T and the parity position are shown in Fig. 2(c). The parity-readout signal does not show any PSB signature, resulting in a constant signal (orange curve). In contrast, the S-T readout shows an exponential decay due to relaxation from a blocked state to the ground state. From this exponential decay, we calculate a characteristic time $T_1 = 0.9$ ms. We interpret this as the signature of the three degenerated triplet states relaxing to the singlet ground state, while at the parity position, due to mixing with the singlet state, the relaxation is faster than the measurement bandwidth and cannot be observed.

To discriminate further between the triplet states, we apply a magnetic field $B_z = 0.3$ T and repeat the same experiment as before with a different initial state. Due to the magnetic field, the triplet degeneracy is lifted and we can prepare a mixed state of S_0, T_0, and T_-. The latter is achieved using the same procedure as before and incorporating a fraction of T_- at the S_0-T_- anticrossing (see Appendix A 5). Figure 2(d) presents the outcome of the readout at the parity and S-T positions for such an initialization. The parity readout results in a single exponential decay with a characteristic relaxation time $T_1 = 32$ ms. We attribute this relaxation to the relaxation of T_-. As in the previous case, T_0 relaxation cannot be resolved due to its high relaxation rate at the parity-measurement position.

The S-T readout shows a double exponential with characteristic relaxation times $T_1 = 0.9$ ms and $T_1 = 32$ ms that we attribute to T_0 and T_- relaxations, respectively, at the S-T–measurement position. It is worth noting that parity readout can also be performed at the S-T readout point. For instance, the use of a time threshold at 3 ms when T_0 has relaxed allows us to obtain information on the remaining T_- population. However, such a measurement leads to poor fidelity in the T_- readout, of approximately 95 %, due to the small contrast between the $T_0 \rightarrow S_0$ and $T_- \rightarrow S_0$ relaxation rates (see Appendix A 3). In the following, we focus on characterization of the parity-readout fidelity.

V. FIDELITY BENCHMARKING OF PARITY READOUT

Here, we want to discuss the optimization of our parity readout, which could also be used to optimize the S-T readout. The readout time is constrained by the relaxation time T_1 at the measurement position. Another parameter to be optimized is the rf power of the readout, which affects the back action on the double dot that can drive relaxation [25]. We benchmark our readout fidelity by varying the rf power as well as the integration time. By performing experiments where we prepare an approximately 50:50 even-odd state ratio by relaxation to the respective ground state, we measure the signal distribution for 10 000 repetitions. The corresponding histogram of the signal distribution for $\tau_m = 20\,\mu$s is shown in Fig. 3(a). We follow Barthel *et al.* [24] in calculating the fidelities by fitting a normal distribution to the signal distribution of the odd state and a normal distribution with a decay term to the signal distribution of the even state (accounting for relaxation during measurement). From the integral of these fits, we calculate the populations of the different states. By plotting the signal-to-noise ratio (SNR) as a function of the power and integration time (see Appendix A 8), we find an optimal power at around −91 dBm. Figure 3 (b) depicts a plot of the fidelities and visibility as a function of integration time τ_m. We find an optimal integration time of $\tau_{\mathrm{m,opt}} = 20\,\mu$s with an odd-even average fidelity of 99.9 %. This results in a visibility of 99.8 %. If we reduce the integration time to 4 µs, which is the limit of our measurement bandwidth, the average fidelity is slightly lower, at 99.6 % for odd-even states and a visibility of 99.1 %, which is still above 99 %. The lower fidelity at short integration times is in good agreement with the expected noise broadening, decreasing the SNR by $\propto \sqrt{\tau_m}$. In the case of S-T readout, a short integration time compared to relaxation gives the same fidelity as for the parity readout. However, for an increasing integration time, it decreases exponentially as T_0 relaxes in the millisecond range; e.g., at 20 µs, it falls below 99 %.

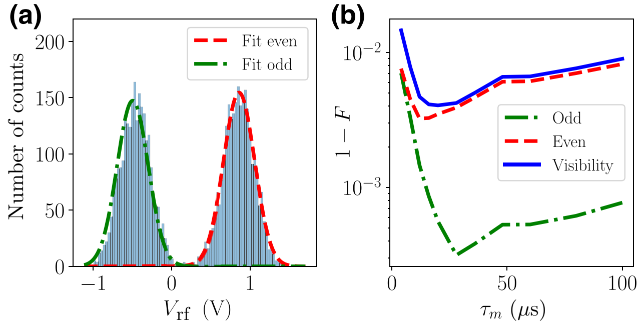

FIG. 3. (a) A histogram of the 10 000 parity-readout measurements at a readout speed of 50 kHz. The state is initialized with an approximately 50 % singlet (triplet) probability. The green (red) curve is a fit to the odd- (even-) state population calculated from the fits to the histograms, following Barthel *et al.* [24]. (b) The fidelity and/or visibility error as a function of the integration time τ_m. The optimal fidelities and visibility are found for $\tau_m = 20\,\mu$s, due to noise-broadening error for faster integration and relaxation error for slower integration.

VI. STATE PREPARATION AND ERROR ANALYSIS

The total fidelity of state preparation and measurement (SPAM) sums up two DiVincenco criteria. We break down the error contributions into three different types: initialization, transfer to the regime of single-qubit operation (1|1), and readout. The latter is characterized in the previous section. To identify the initialization error, we start by initializing in (1|0) and load a second electron into $\mathrm{QD_{B2}}$ by pulsing into (2|0), where we allow relaxation to the ground state by waiting for 10 ms. Then, we pulse after this initialization phase to the readout measurement position and measure the spin state. We find the signal distribution depicted in Fig. 4(a), indicating a S_0 initialization fidelity of 99.6 %.

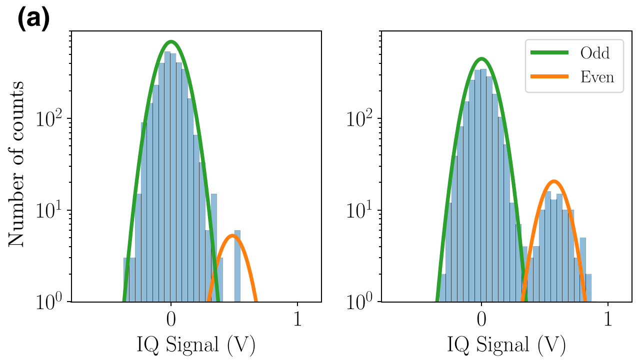

FIG. 4. (a) A histogram of the S_0 initialization. (b) A histogram of an initialized S_0, followed by a transfer to (1|1) with a direct return to the measurement position.

We now investigate errors due to transfer in (1|1), where the two electrons can be decoupled. We initialize a singlet state in (0|2) as previously described. We then transfer one electron by performing first a nonadiabatic pulse to avoid the S_0-T_- anticrossing (see Appendix A 5) followed by an adiabatic ramp deep in (1|1) to avoid mixing S_0 with T_0. Without waiting, we pulse from this position to the measurement position. Considering the time per instruction in our sequence, the total time spent in (1|1) is approximately 20 µs, which is negligible with regard to the relaxation time $T_1 > 1$ s in (1|1) (see Appendix A 4). We find a S_0 population of 95.6 % for the transfer measurement by using the signal distribution depicted in Fig. 4(b). We attribute the 4 % difference between these two experiments to leakage during the transfer through the S_0-T_- anticrossing. This assumption is supported by a Landau-Zener type of experiment where the transfer from (0|2) to (1|1) is performed at different detuning sweep rate (see Appendix A 5). The presence of the anticrossing leads to a sweep-rate-dependent singlet probability.

VII. CONCLUSIONS

We show how we can operate a triple quantum dot to perform high-fidelity single-shot readout of a double quantum dot system. Due to a strong capacitive coupling and reflectometry method, we are able to achieve spin-readout fidelities above 99.9 % (99 %) in 20 µs (4 µs). Using the spin readout, we characterize the different error sources during initialization and displacement of electrons between the (2|0) and (1|1) regimes. Finally, by adjusting the measurement position in detuning, we can alternatively use singlet-triplet or parity readout. The sequential combination of these two readouts can be of strong interest in order to extract the full spin information of a two-qubit system. As proposed in Ref. [13], to achieve such complete readout, we could start with a S-T readout to distinguish the singlet from all triplets. Followed by a parity readout, this would allow us to distinguish the unpolarized triplet (T_0) from the two polarized ones (T_- and T_+). Finally, an adiabatic transfer that swaps the T_- and S_0 population followed by a S-T or parity readout would allow us to differentiate between the two polarized triplets.

ACKNOWLEDGMENTS

We acknowledge support for the cryogenic apparatus from W. Wernsdorfer, E. Bonet, and E. Eyraud. We acknowledge technical support from L. Hutin, D. Lepoittevin, I. Pheng, T. Crozes, L. Del Rey, D. Dufeu, J. Jarreau, C. Hoarau, and C. Guttin. D.J.N. acknowledges the Grenoble Quantum Engineering (GreQuE) doctoral programs (Grant Agreement No. 754303). The device fabrication is funded through the Mosquito project (Grant Agreement No. 688539). This work is supported by the Agence Nationale de la Recherche through the CRYMCO project (Grant No. ANR-20-CE24-009) and the CMOSQSPIN project (Grant No. ANR-17-CE24-0009). This project also receives funding from the QuCube project (Grant Agreement No. 810504) and the "Quantum Large-Scale Integration" (QLSI) project (Grant Agreement No. 951852).

Note added.—We have recently become aware of an experimental observation of a PSB in a similar device [26].

APPENDIX

1. Charge state of double quantum dot system

We measure a stability diagram of the two potential sensing dots to decide which one we use as a sensing dot. The stability diagram is depicted in Fig. 5(a), with enlargements of the regions of interest in Figs. 5(b) and 5(c) for $\mathrm{QD_{B1}}$ and $\mathrm{QD_{T1}}$, respectively. We use $\mathrm{QD_{B1}}$ as a sensing dot as it shows a strong signal at a low number of electrons.

The use of the charge-degeneracy points of the sensing dot as a charge sensor for the two center quantum dots allows us to determine the number of charges in the quantum dots. Figure 6 depicts three stability diagrams for different sensor voltages. The transitions of $\mathrm{QD_{B2}}$ ($\mathrm{QD_{T2}}$) are indicated as orange (red) lines in Fig. 6(d) allows us to map out all transitions of the sensed dots by overlaying 20 stability diagrams. The use of multiple degeneracy points of the sensor allows us to identify the different charge regimes in a single stability diagram, as depicted in Fig. 6(e) (here, T1 is used as sensor). In the main text, we use the first degeneracy point of the QD defined by B1 as sensor. In this configuration, the sensor is weakly tunnel coupled to the QD of T2, reducing the lifting of PSB by cotunneling through the sensor dot.

2. Signal demodulation

The IQ demodulation, which we perform after the signal reflection, results in signals of the I and Q quadratures. Preparing a population with an approximately 50:50 probability of an even or odd state, we measure 2000 single-shot

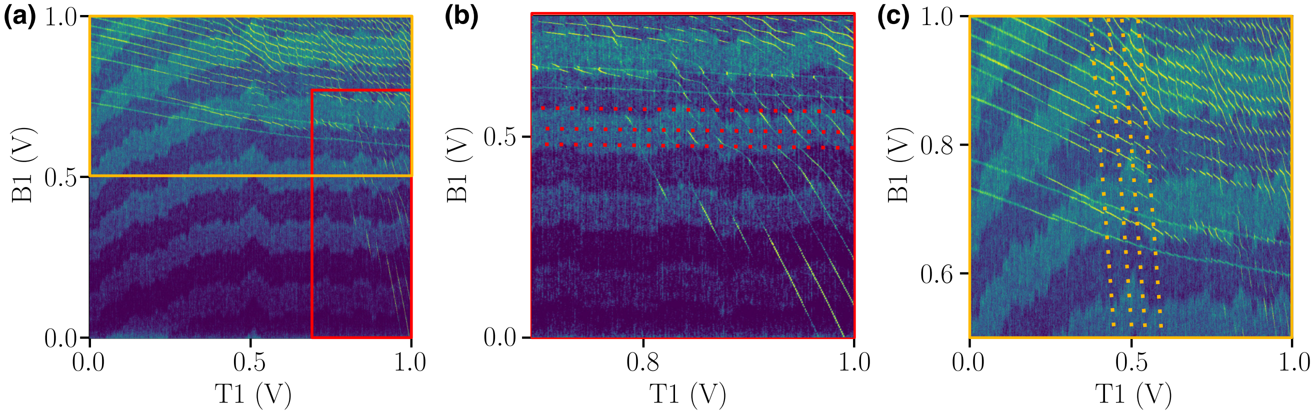

FIG. 5. (a) The charge-stability diagram of the two sensing dots, $\mathrm{QD}_{\mathrm{B1}}$ and $\mathrm{QD}_{\mathrm{T1}}$. (b) An enlargement of the region in the red rectangle in (a), with indicated transitions of $\mathrm{QD}_{\mathrm{B1}}$, sensed by $\mathrm{QD}_{\mathrm{T1}}$. (c) An enlargement of the region in the orange rectangle in (a), with indicated transitions of $\mathrm{QD}_{\mathrm{T1}}$, sensed by $\mathrm{QD}_{\mathrm{B1}}$.

measurements and plot a histogram of the signal distribution, depicted in Fig. 8. The even and odd signal distributions follow 2D normal distributions. We indicate the two normal distributions with white dashed circles. Adjusting the relative phase, we can tune the demodulation such that all the information is in the I quadrature. This allows us to ignore the Q quadrature and we can set our measurement bandwidth twice as high as when we are measuring both quadratures.

3. Fidelity and visibility definitions

Following the analysis of Barthel *et al.* [24], we fit the signal distribution of the PSB measurement using the following:

$$n_S(V_{\mathrm{rf}}) = \frac{1-\langle P_T\rangle}{\sqrt{2\pi}\sigma}e^{-(V_{\mathrm{rf}}-V_{\mathrm{rf}}^S)^2/2\sigma^2}, \tag{A1}$$

$$\begin{aligned} n_T(V_{\mathrm{rf}}) = {}& \frac{\langle P_T\rangle}{\sqrt{2\pi}\sigma}e^{-\tau_m/T_1}e^{-(V_{\mathrm{rf}}-V_{\mathrm{rf}}^T)^2/2\sigma^2} \\ & + \int_{V_{\mathrm{rf}}^S}^{V_{\mathrm{rf}}^T}\frac{\tau_m}{T_1}\frac{\langle P_T\rangle}{\Delta V_{\mathrm{rf}}}e^{-V-V_{\mathrm{rf}}^S/\Delta V_{\mathrm{rf}}\frac{\tau_m}{T_1}}e^{-(V_{\mathrm{rf}}-V)^2/2\sigma^2} \\ & \times\frac{dV}{\sqrt{2\pi}\sigma}, \end{aligned} \tag{A2}$$

where $\langle P_T\rangle$ is the triplet probability, V_{rf}^S (V_{rf}^T) is the signal expectation value for the nonblocked (blocked) state, σ is the standard deviation of the Gaussian signal distribution, τ_m is the measurement integration time, and T_1 is the lifetime at the measurement position. While Eq. (A1) is a Gaussian distribution, describing the nonblocked state signal distribution, the excited state is given by Eq. (A2), the convolution of a Gaussian distribution with an exponential decay. We use these functions to fit the signal distribution of our PSB measurements. An example is given in Fig. 7(a).

The definition of the fidelities allows a simple metric to estimate the error of the signal assignment as blocked (nonblocked). The singlet and triplet fidelities are defined as

$$F_S = 1-\int_{V_T}^{\infty}n_S(V)dV, \tag{A3}$$

$$F_T = 1-\int_{-\infty}^{V_T}n_T(V)dV,, \tag{A4}$$

where V_T is the threshold that separates the identification as either the blocked or the nonblocked state. The visibility is then defined as

$$V = F_S + F_T - 1. \tag{A5}$$

To optimize the threshold, one calculates the maximum of the visibility. Figure 7(b) depicts the error of the fidelities and visibility for the fits from Fig. 7(a) close to the maximal visibility.

4. Lifetime of S_0 in (1|1)

While we initialize in the S_0 state, spin operations take place in the (1|1) regime, where T_- is the ground state. Therefore, the relaxation of S_0 in (1|1) must be much slower than the spin manipulation. We measure the S_0 relaxation by preparing a S_0 state, followed by pulsing in the (1|1) regime. Deep in the (1|1) regime, where we can assume that the quantum dots are completely decoupled, we wait for a given time τ ranging from 0.1 ms to 3 s. Then, we pulse to the parity-readout position and measure the spin state. We fit the resulting signal distribution from 2000 data traces. The T_- (T_+) population from these measurements is depicted in Fig. 9. We fit an exponential function with a decay time $T_1 \approx 1.6$ s. This relaxation time is much longer than typical times of operation in (1|1), which are usually no longer than a few μs, around 6 orders

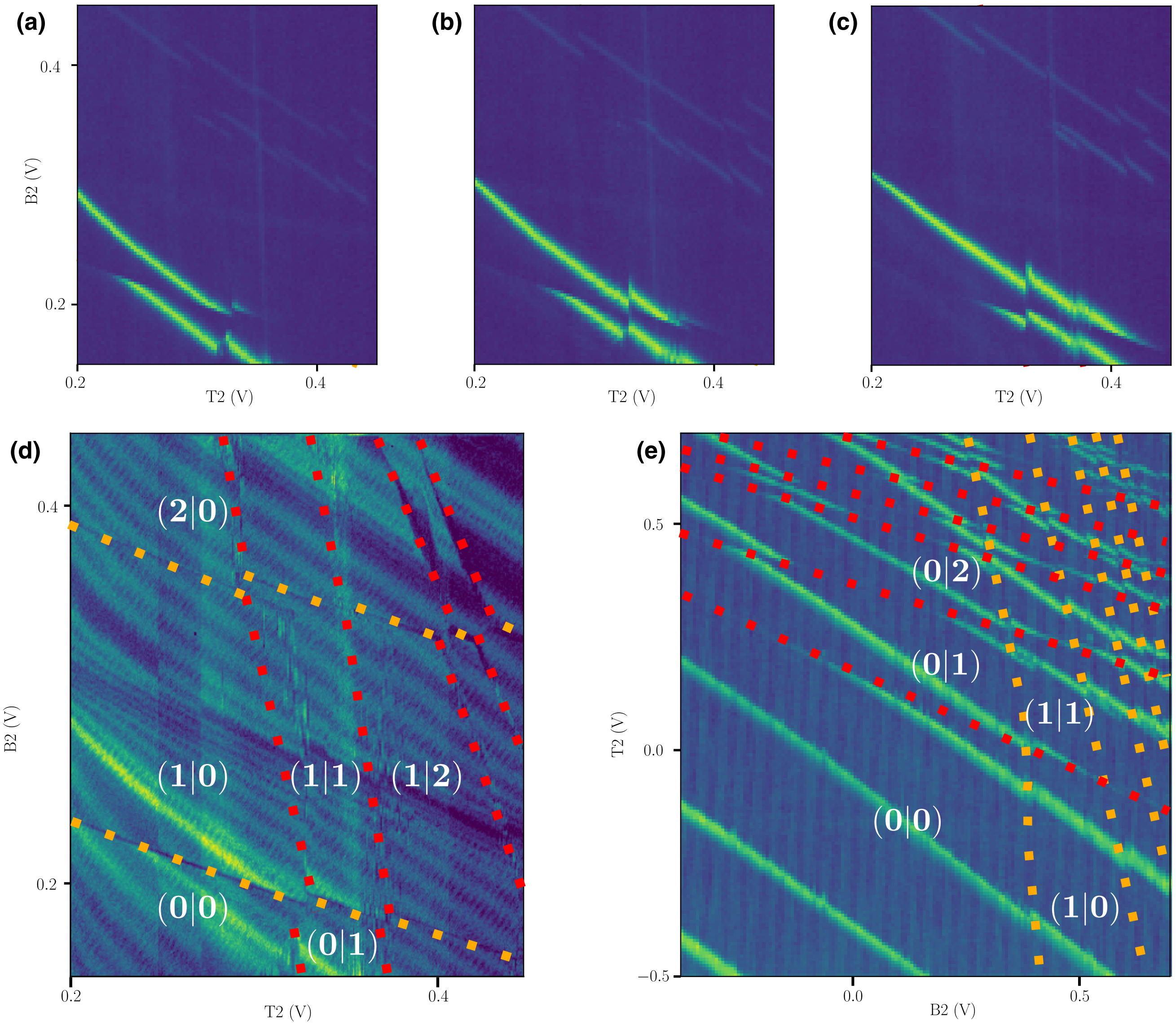

FIG. 6. (a) The stability diagram of the two gates B2 and T2 with the sensor B1 set to 0.662 V. A single charge-degeneracy line of the sensor is visible. When a charge transition of one of the two QDs, B2 or T2, is aligned with the sensor degeneracy point, the sensor line shows a sharp horizontal (vertical) discontinuity for a transition of B2 (T2). (b),(c) The same stability diagram with the gate voltage on the sensor gate set to 0.6615 V and 0.661 V, respectively. (d) The overlap of 20 stability diagrams with the sensor gate voltage ranging from 0.67 V to 0.657 V. (e) The stability diagram using $\mathrm{QD}_{\mathrm{T1}}$ as sensor. The use of multiple sensor degeneracy points in a single stability diagram allows identification of the charge regimes of the double quantum dot system.

of magnitude shorter than the relaxation time. The high temperature of operation compared to the magnetic field of 150 mT leads to a relatively high residual S_0 population in this experiment.

5. Landau-Zener experiment

The transfer from the (2|0) regime to the (1|1) involves the passage of the S_0 - T_- anticrossing for $B_z \neq 0$. We perform a Landau-Zener experiment to estimate the fraction of nonadiabatic transfer. We initialize in S_0 and ramp with amplitude $\Delta\epsilon$ from (2|0) to (1|1) and return nonadiabatically to the measurement position. The pulse schematic is depicted in the inset in Fig. 10. We perform this experiment with different ramp speeds and calculate the transfer speed as $\nu = \alpha e \Delta\epsilon/\tau$, where α and e are the gate lever arm and elementary charge, respectively. The experiment is performed at a base temperature of 100 mK and a magnetic field B_z = 300 mT. We find the expected monotonous increase of singlet conservation with higher transfer speed and extract a S_0-T_- avoided crossing of 120 MHz. For very slow transfer, the population tends toward more and more population of the triplet ground state. The residual S_0 population could arise from

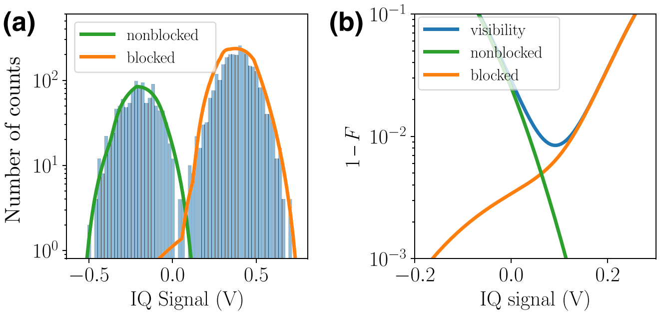

FIG. 7. (a) A histogram of the 10 000 single-shot traces at the parity-readout position: the fitted distribution of the blocked (orange) and nonblocked (green) states. (b) The fidelity and visibility error defined as $1-F$ for the fits in (a).

charge noise, which induces rapid fluctuations in the vicinity of the anticrossing, reducing the maximum transfer probability [27].

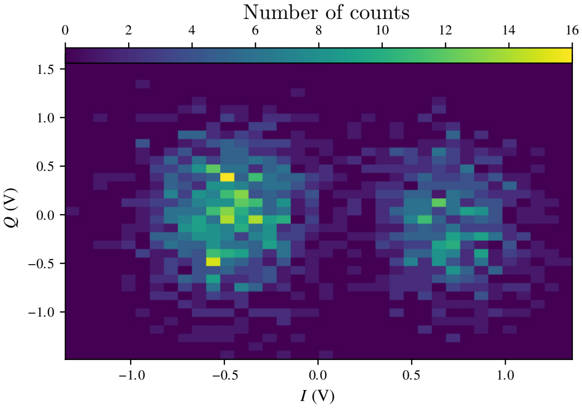

FIG. 8. The IQ-signal histogram of 2000 single-shot measurements. The state is prepared with an approximately 50:50 probability in an even or odd state. The two dashed circles highlight the signals for the two states.

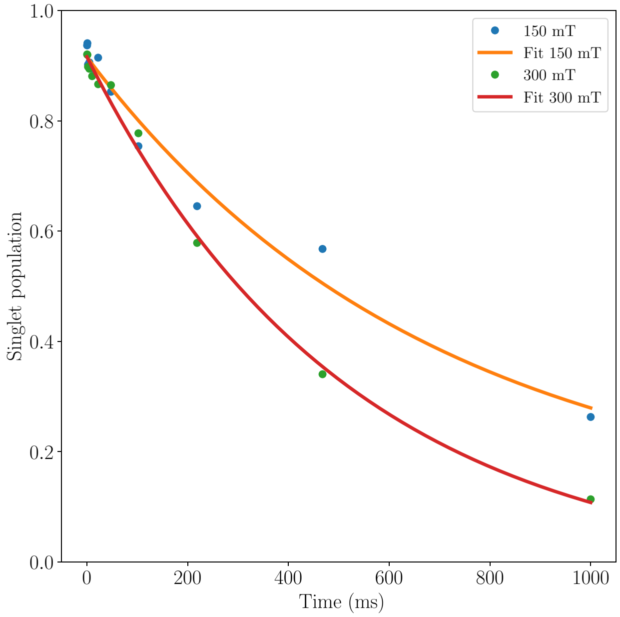

FIG. 9. The singlet population as a function of the waiting time in (1|1) for a magnetic field of 150 mT (blue dots) and 300 mT (green dots). The fitted S_0 relaxation for 150 mT (orange) [300 mT (red)] giving a lifetime of $T_1 \approx 640$ ms (520 ms).

6. Measuring gate lever arm

We determine the lever arm using the method proposed by Rossi *et al.* [28]. We average traces along the charge transition of T2 indicated in Fig. 11(a). The conversion between the gate voltage and the dot potential is given by

$$E - E_0 = \alpha e (V_G - V_0), \tag{A6}$$

where E is the energy, E_0 is the energy of the system at the charge-degeneracy point, α is the gate lever arm, e is the elementary charge, and V_G is the gate voltage with respect to the voltage of the degeneracy point of the charge transition V_0. For this transition, the condition $E_C \gg k_B T_e \gtrsim \Delta\epsilon$, where E_C is the charging energy, k_B is the Boltzmann constant, T_e is the electron temperature, and $\Delta\epsilon$ is the single-particle level separation, is fulfilled. We can thus approximate the transition broadening using the

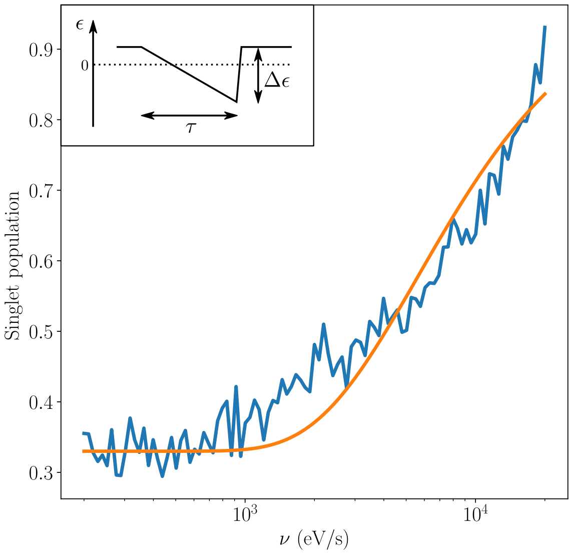

FIG. 10. The singlet population as a function of the transfer speed. The inset shows a schematic pulse sequence of the Landau-Zener experiment. While we keep the amplitude $\Delta\epsilon$ constant, we vary the ramp time τ. The transfer speed is then calculated from $\nu = \alpha e \Delta\epsilon/\tau$, where α and e are the gate lever arm and elementary charge, respectively.

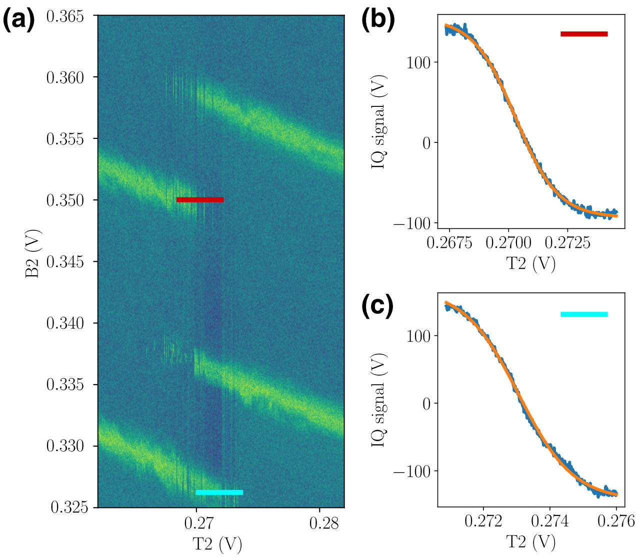

FIG. 11. (a) The stability diagram showing a charge transition of T2. (b),(c) Traces along the charge-degeneracy point of $\mathrm{QD}_{\mathrm{T2}}$ and a respective fit (orange) to the sensor signal. The depicted traces are averaged over 500 measurements.

Fermi-Dirac distribution:

$$f(E-E_0) = \frac{1}{1+e^{-(E-E_0)/k_B T_e}} = \frac{1}{1+e^{\alpha e (V_G-V_0)/k_B T_e}}. \tag{A7}$$

From the charge-transition fits in Figs. 11(b) and 11(c), we extract a gate lever arm of $\alpha = 0.050 \pm 0.002$.

7. Spin-funnel experiment

Using a second device with the same geometry and from the same wafer, we tune it to the two-electron regime and perform a spin-funnel experiment following Ref. [29]. As a result of this experiment, we plot the probability of measuring a (1|1) signal (even state) as a function of the pulse amplitude along the detuning axis ϵ and the magnetic field B_z in Fig. 12. For the initialization of a singlet state, we wait for relaxation to the ground state in (2|0). Next, we apply a DAC pulse on B2 with a duration of 10 ms. We scan the interdot transition by varying the B2 pulse amplitude and calculate the probability of measuring (1|1) from 2000 single-shot measurements, as depicted in Fig. 12. The long pulse duration results in a high (1|1) probability after crossing the S_0-T_- anticrossing due to relaxation to the ground state. The (1|1) probability indicates the characteristic funnel-shaped shift of the S_0-T_- avoided crossing with an increasing magnetic field.

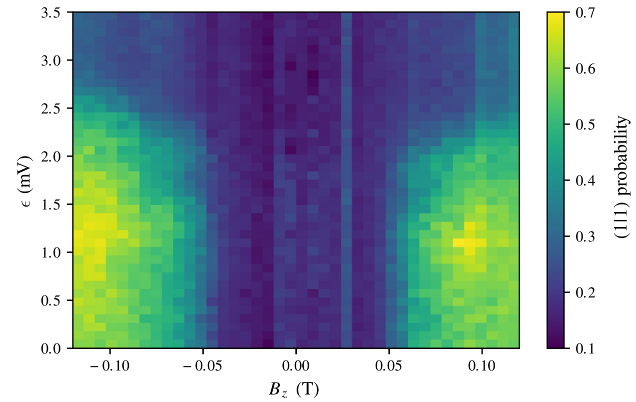

FIG. 12. The probability of measuring a (1|1) signal as a function of the magnetic field and pulse amplitude along the detuning axis ϵ. We initialize a singlet state by waiting for relaxation to the ground state in (2|0). Then, we pulse for 10 ms to the dwell position, followed by a pulse to the measurement position, where the signal is detected.

8. Reflectometry back action

We investigate the back action of the sensing mechanism on the spin state by performing fidelity measurements as a function of the rf power. We find that for > -100 dBm, the lifetime at the measurement position is strongly decreased by one order of magnitude [see Figs. 13(a) and 13(b)]. However, increasing the rf power

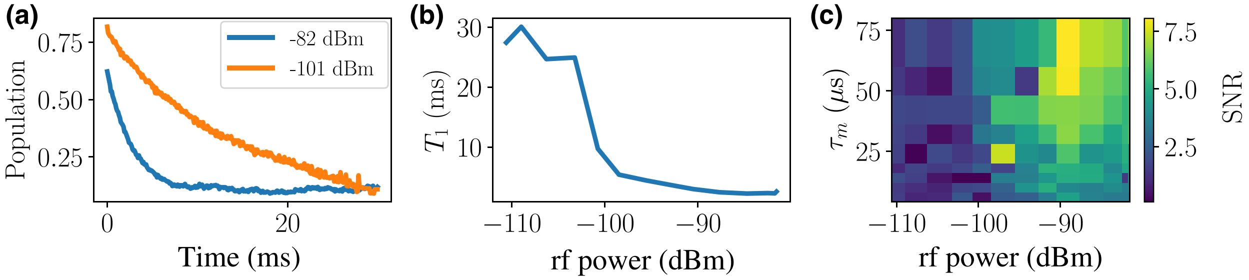

FIG. 13. (a) The relaxation of the even state at the parity-readout position for rf power levels of -71 dBm and -91 dBm. The relaxation is faster for the higher rf power. (b) The lifetime T_1 of even states as a function of the rf input power at the parity-readout position. The graph shows a sharp decrease in T_1 of one order of magnitude around -100 dBm. (c) The SNR as a function of the integration time τ_m and the rf power.

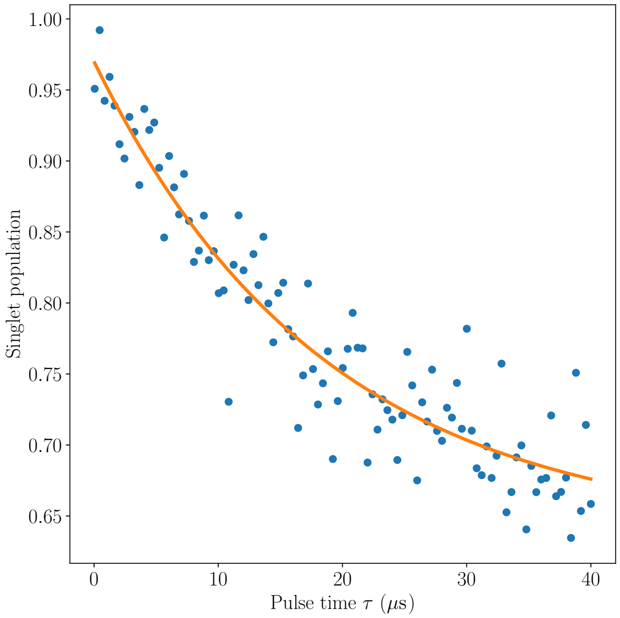

FIG. 14. The singlet population as a function of the pulse duration measured at the S-T readout position. The square pulse is applied to gate B2 to move the electrons from the (0|2) to the (1|1) regime. We interpret the decay as a mixing between the S and T_0 states with a characteristic time of 18.5 ±2.5 μs, in agreement with the spin decoherence in isotopically purified ^{28}Si measured in [30].

goes along with an increase in the signal strength. We map the SNR as a function of the rf power and the integration time in Fig. 13(c). The best SNR is found at around −90 dBm, where the lifetime T_1 at the measurement position is approximately 3 ms.

9. S_0-T_0 mixing

To prepare a mixed $T_0(1|1)$, $S_0(1|1)$ state, we start by preparing a singlet state through relaxation to the ground state in (0|2). Then, we pulse the T2 and B2 gates to the measurement position of the S-T readout, followed by a square pulse on the B2 gate to move electrons deep into (1|1). After the AWG pulse, we measure the spin state using PSB at the S-T readout. We plot the singlet population as a function of the pulse duration in Fig. 14. The singlet population as a function of the pulse duration can be fitted with an exponential decay, indicating a characteristic time scale of 18.5 ±2.5 μs. The exponential decay and the convergence toward a population of 50 % are indications that $S_0(1|1)$ and $T_0(1|1)$ mixing occurs. However, no spin-orbit-induced coherent oscillations are observed. This could be explained by a quenched difference of the *g* factor when the magnetic field is applied perpendicular to the nanowire axis, as found in the planar MOS silicon double quantum dot with the magnetic field perpendicular to the plane [31].

[1] S. G. J. Philips, M. T. Mądzik, S. V. Amitonov, S. L. de Snoo, M. Russ, N. Kalhor, C. Volk, W. I. L. Lawrie, D. Brousse, L. Tryputen, B. P. Wuetz, A. Sammak, M. Veldhorst, G. Scappucci, and L. M. K. Vandersypen, Universal control of a six-qubit quantum processor in silicon (2022).

[2] N. W. Hendrickx, W. I. L. Lawrie, M. Russ, F. van Riggelen, S. L. de Snoo, R. N. Schouten, A. Sammak, G. Scappucci, and M. Veldhorst, A four-qubit germanium quantum processor, Nature **591**, 580 (2021).

[3] M. Veldhorst, H. G. J. Eenink, C. H. Yang, and A. S. Dzurak, Silicon CMOS architecture for a spin-based quantum computer, Nat. Commun. **8**, 1766 (2017).

[4] A. Ruffino, T.-Y. Yang, J. Michniewicz, Y. Peng, E. Charbon, and M. F. Gonzalez-Zalba, A cryo-CMOS chip that integrates silicon quantum dots and multiplexed dispersive readout electronics, Nat. Electron. **5**, 53 (2021).

[5] X. Xue, *et al.*, CMOS-based cryogenic control of silicon quantum circuits, Nature **593**, 205 (2021).

[6] M. Urdampilleta, D. J. Niegemann, E. Chanrion, B. Jadot, C. Spence, P.-A. Mortemousque, C. Bäuerle, L. Hutin, B. Bertrand, S. Barraud, R. Maurand, M. Sanquer, X. Jehl, S. D. Franceschi, M. Vinet, and T. Meunier, Gate-based high fidelity spin readout in a CMOS device, Nat. Nanotechnol. **14**, 737 (2019).

[7] C. H. Yang, R. C. C. Leon, J. C. C. Hwang, A. Saraiva, T. Tanttu, W. Huang, J. C. Lemyre, K. W. Chan, K. Y. Tan, F. E. Hudson, K. M. Itoh, A. Morello, M. Pioro-Ladrière, A. Laucht, and A. S. Dzurak, Operation of a silicon quantum processor unit cell above one kelvin, Nature **580**, 350 (2020).

[8] L. C. Camenzind, S. Geyer, A. Fuhrer, R. J. Warburton, D. M. Zumbühl, and A. V. Kuhlmann, A hole spin qubit in a fin field-effect transistor above 4 kelvin, Nat. Electron. **5**, 178 (2022).

[9] L. Petit, H. G. J. Eenink, M. Russ, W. I. L. Lawrie, N. W. Hendrickx, S. G. J. Philips, J. S. Clarke, L. M. K. Vandersypen, and M. Veldhorst, Universal quantum logic in hot silicon qubits, Nature **580**, 355 (2020).

[10] L. Petit, J. M. Boter, H. G. J. Eenink, G. Droulers, M. L. V. Tagliaferri, R. Li, D. P. Franke, K. J. Singh, J. S. Clarke, R. N. Schouten, V. V. Dobrovitski, L. M. K. Vandersypen, and M. Veldhorst, Spin Lifetime and Charge Noise in Hot Silicon Quantum Dot Qubits, Phys. Rev. Lett. **121**, 076801 (2018).

[11] F. Borjans, X. Mi, and J. Petta, Spin Digitizer for High-Fidelity Readout of a Cavity-Coupled Silicon Triple Quantum Dot, Phys. Rev. Appl. **15**, 044052 (2021).

[12] J. Z. Blumoff, *et al.*, Fast and High-Fidelity State Preparation and Measurement in Triple-Quantum-Dot Spin Qubits, PRX Quantum **3**, 010352 (2022).

[13] M. Nurizzo, B. Jadot, P.-A. Mortemousque, V. Thiney, E. Chanrion, D. Niegemann, M. Dartiailh, A. Ludwig, A. D. Wieck, C. Bäuerle, M. Urdampilleta, and T. Meunier, Complete readout of two-electron spin states in a double quantum dot (2022),.

[14] A. E. Seedhouse, T. Tanttu, R. C. Leon, R. Zhao, K. Y. Tan, B. Hensen, F. E. Hudson, K. M. Itoh, J. Yoneda, C. H. Yang, A. Morello, A. Laucht, S. N. Coppersmith, A. Saraiva, and A. S. Dzurak, Pauli Blockade in Silicon Quantum Dots with Spin-Orbit Control, PRX Quantum **2**, 010303 (2021).

[15] N. Rohling and G. Burkard, Tomography scheme for two spin-1/2 qubits in a double quantum dot, Phys. Rev. B **88,** 085402 (2013).

[16] M. G. House, T. Kobayashi, B. Weber, S. J. Hile, T. F. Watson, J. van der Heijden, S. Rogge, and M. Y. Simmons, Radio frequency measurements of tunnel couplings and singlet-triplet spin states in Si:P quantum dots, Nat. Commun. **6,** 8848 (2015).

[17] P.-A. Mortemousque, E. Chanrion, B. Jadot, H. Flentje, A. Ludwig, A. D. Wieck, M. Urdampilleta, C. Bäuerle, and T. Meunier, Coherent control of individual electron spins in a two-dimensional quantum dot array, Nat. Nanotechnol. **16,** 296 (2021).

[18] A. Cottet, C. Mora, and T. Kontos, Mesoscopic admittance of a double quantum dot, Phys. Rev. B **83,** 121311 (2011).

[19] E. Chanrion, D. J. Niegemann, B. Bertrand, C. Spence, B. Jadot, J. Li, P.-A. Mortemousque, L. Hutin, R. Maurand, X. Jehl, M. Sanquer, S. D. Franceschi, C. Bäuerle, F. Balestro, Y.-M. Niquet, M. Vinet, T. Meunier, and M. Urdampilleta, Charge Detection in an Array of CMOS Quantum Dots, Phys. Rev. Appl. **14,** 024066 (2020).

[20] F. Ansaloni, A. Chatterjee, H. Bohuslavskyi, B. Bertrand, L. Hutin, M. Vinet, and F. Kuemmeth, Single-electron operations in a foundry-fabricated array of quantum dots, Nat. Commun. **11,** 6399 (2020).

[21] M. G. House, I. Bartlett, P. Pakkiam, M. Koch, E. Peretz, J. van der Heijden, T. Kobayashi, S. Rogge, and M. Y. Simmons, High-Sensitivity Charge Detection with a Single-Lead Quantum Dot for Scalable Quantum Computation, Phys. Rev. Appl. **6,** 044016 (2016).

[22] M. F. Gonzalez-Zalba, S. Barraud, A. J. Ferguson, and A. C. Betz, Probing the limits of gate-based charge sensing, Nat. Commun. **6,** 6084 (2015).

[23] C. Spence, B. C. Paz, B. Klemt, E. Chanrion, D. J. Niegemann, B. Jadot, V. Thiney, B. Bertrand, H. Niebojewski, P.-A. Mortemousque, X. Jehl, R. Maurand, S. De Franceschi, M. Vinet, F. Balestro, C. Bäuerle, Y.-M. Niquet, T. Meunier, and M. Urdampilleta, Spin-Valley Coupling Anisotropy and Noise in CMOS Quantum Dots, Phys. Rev. Appl. **17,** 034047 (2022).

[24] C. Barthel, D. J. Reilly, C. M. Marcus, M. P. Hanson, and A. C. Gossard, Rapid Single-Shot Measurement of a Singlet-Triplet Qubit, Phys. Rev. Lett. **103,** 160503 (2009).

[25] D. J. Reilly, C. M. Marcus, M. P. Hanson, and A. C. Gossard, Fast single-charge sensing with a rf quantum point contact, Appl. Phys. Lett. **91,** 162101 (2007).

[26] G. A. Oakes, V. Ciriano-Tejel, D. Wise, M. A. Fogarty, T. Lundberg, C. Laine, S. Schaal, F. Martins, D. J. Ibberson, L. Hutin, B. Bertrand, N. Stelmashenko, J. A. W. Robinson, L. Ibberson, A. Hashim, I. Siddiqi, A. Lee, M. Vinet, C. G. Smith, J. Morton, and M. F. Gonzalez-Zalba, Fast high-fidelity single-shot readout of spins in silicon using a single-electron box. In: Arxiv (2022),.

[27] J. M. Nichol, S. P. Harvey, M. D. Shulman, A. Pal, V. Umansky, E. I. Rashba, B. I. Halperin, and A. Yacoby, Quenching of dynamic nuclear polarization by spin-orbit coupling in GaAs quantum dots, Nat. Commun. **6,** 7682 (2015).

[28] A. Rossi, T. Ferrus, and D. A. Williams, Electron temperature in electrically isolated Si double quantum dots, Appl. Phys. Lett. **100,** 133503 (2012).

[29] M. A. Fogarty, K. W. Chan, B. Hensen, W. Huang, T. Tanttu, C. H. Yang, A. Laucht, M. Veldhorst, F. E. Hudson, K. M. Itoh, D. Culcer, T. D. Ladd, A. Morello, and A. S. Dzurak, Integrated silicon qubit platform with single-spin addressability, exchange control and single-shot singlet-triplet readout, Nat. Commun. **9,** 4370 (2018).

[30] P. Harvey-Collard, N. T. Jacobson, C. Bureau-Oxton, R. M. Jock, V. Srinivasa, A. M. Mounce, D. R. Ward, J. M. Anderson, R. P. Manginell, J. R. Wendt, T. Pluym, M. P. Lilly, D. R. Luhman, M. Pioro-Ladrière, and M. S. Carroll, Spin-Orbit Interactions for Singlet-Triplet Qubits in Silicon, Phys. Rev. Lett. **122,** 217702 (2019).

[31] T. Tanttu, B. Hensen, K. W. Chan, C. H. Yang, W. W. Huang, M. Fogarty, F. Hudson, K. Itoh, D. Culcer, A. Laucht, A. Morello, and A. Dzurak, Controlling Spin-Orbit Interactions in Silicon Quantum Dots Using Magnetic Field Direction, Phys. Rev. X **9,** 021028 (2019).